

© 2019 by Akshat Puri. All rights reserved.

MEASUREMENT OF ANGULAR AND MOMENTUM DISTRIBUTIONS OF CHARGED
PARTICLES WITHIN AND AROUND JETS IN Pb+Pb AND $p\bar{p}$ COLLISIONS AT
 $\sqrt{S_{NN}} = 5.02$ TeV WITH ATLAS AT THE LHC

BY
AKSHAT PURI

DISSERTATION

Submitted in partial fulfillment of the requirements
for the degree of Doctor of Philosophy in Physics
in the Graduate College of the
University of Illinois at Urbana-Champaign, 2019

Urbana, Illinois

Doctoral Committee:

Professor Matthias Grosse Perdekamp, Chair
Professor Anne Marie Sickles, Advisor
¹ Professor Aida El-Khadra
Professor Bryce Gadaway

Abstract

² Studies of the fragmentation of jets into charged particles in heavy-ion collisions can help in understanding
³ the mechanism of jet quenching by the hot and dense matter created in such collisions, the quark-gluon
⁴ plasma. This thesis presents a measurement of the angular distribution of charged particles around the jet
⁵ axis as measured in Pb+Pb and pp collisions collided at a center of mass energy of $\sqrt{s_{NN}} = 5.02$ TeV. The
⁶ measurement is done using the ATLAS detector at the Large Hadron Collider, and utilizes 0.49 pb^{-1} of
⁷ Pb+Pb and 25 pb^{-1} of pp data collected in 2015. The measurement is performed for jets reconstructed
⁸ with the anti- k_t algorithm with radius parameter $R = 0.4$, and is extended to regions outside the jet cone.
⁹ Results are presented as a function of Pb+Pb collision centrality, and both jet and charged-particle transverse
¹⁰ momenta. It was observed that in Pb+Pb collisions there is a broadening of the jet for charged particles with
¹¹ $p_T < 4$ GeV, along with a narrowing for charged particles with $p_T > 4$ GeV. Ratios between the angular
¹² distributions in Pb+Pb and pp showed an enhancement for particles with $p_T < 4$ GeV in Pb+Pb collisions,
¹³ with the enhancement increasing up to 2 for $r < 0.3$, and remaining constant for $0.3 < r < 0.6$. Charged
¹⁴ particles with $p_T > 4$ GeV show a small enhancement in the jet core for $r < 0.05$, with a growing suppression
¹⁵ of up to 0.5 for $r < 0.3$ in Pb+Pb collisions. The depletion remains constant for $0.3 < r < 0.6$.

For my Mother, Father, and Brother

¹⁸ Contents

¹⁹	Chapter 1 Theoretical Introduction	1
²⁰	1.1 Quantum Chromodynamics	1
²¹	1.2 Heavy Ion Collisions	4
²²	1.3 Quark Gluon Plasma	9
²³	1.4 Jets and Jet Quenching	11
²⁴	1.4.1 Jet Reconstruction	15
²⁵	Chapter 2 Major Jet Measurements	19
²⁶	2.1 Modification of jet yields: Jet R_{AA}	19
²⁷	2.2 Jet X_J	19
²⁸	2.3 Jet Fragmentation	19

Chapter 1

Theoretical Introduction

This section shall discuss the theoretical background necessary to understand jet measurements. It will discuss the fundamentals of quantum chromodynamics (QCD), the heavy ion collision system and the quark gluon plasma that is formed, and finally jets and jet energy loss.

1.1 Quantum Chromodynamics

Quantum Chromodynamics is a gauge theory with SU(3) symmetry that describes the dynamics of the strong interactions between quarks and gluons. It is part of the Standard Model [1], the building blocks of which are shown in Figure 1.1.

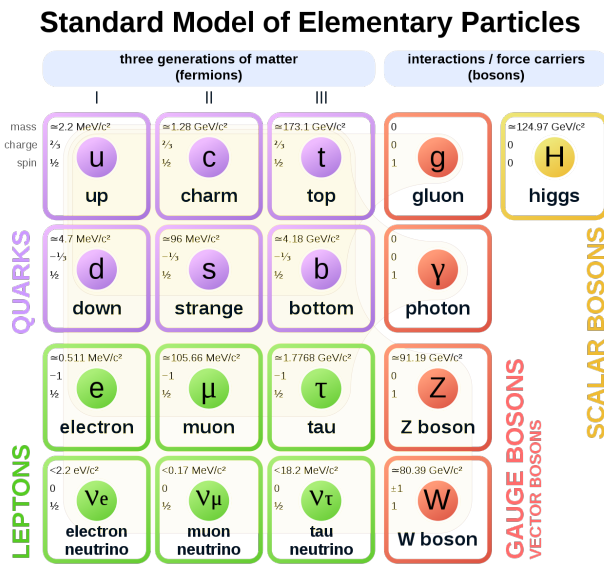


Figure 1.1: The elementary particles of the standard model.

Quarks are fermions with a spin of 1/2, and carry a fractional electric charge as well as a color charge. They all have mass and come in six flavors: up, down, top, bottom, strange, charm. The lightest quarks

³⁸ (u and d) combine and form stable particles, while the heavier quarks can only be produced in energetic
³⁹ environments and decay rapidly. Gluons are gauge bosons (force carriers) with a spin of 1, and are what hold
⁴⁰ quarks together. The dynamics of the quarks and gluons are described by the QCD Lagrangian given as [2]:

$$\mathcal{L}_{\text{QCD}} = \sum_q \bar{\psi}_{q,a} (i\gamma^\mu \partial_\mu \delta_{ab} - g_s \gamma^\mu t_{ab}^C \mathcal{A}_\mu^C - m_q \delta_{ab}) \psi_{q,b} - \frac{1}{4} F_{\mu\nu}^A F^{A\mu\nu} \quad (1.1)$$

⁴¹ where $\psi_{q,a}$ and $\psi_{q,b}$ are quark-filled spinors for a quarks with flavor q , mass m_q , and color a and b respectively,
⁴² with the values for a and b ranging from 1 to 3 (for the three colors). The \mathcal{A}_μ^C corresponds to the gluon field
⁴³ with C taking values from 1 through 8 (for the 8 types of gluons). The t_{ab}^C corresponds to the Gell-Mann
⁴⁴ matrices that are the generators of the SU(3) group, and dictate the rotation of the quarks color in SU(3)
⁴⁵ space when it interacts with a gluon. The coupling constant is encoded within g_s , which is defined by
⁴⁶ $g_s \equiv \sqrt{4\pi\alpha_s}$. The field tensor $F_{\mu\nu}^A$ can be written in terms of the structure constants of the SU(3) group
⁴⁷ f_{ABC} , and is given by:

$$F_{\mu\nu}^A = \partial_\mu \mathcal{A}_\nu^A - \partial_\nu \mathcal{A}_\mu^A - g_s f_{ABC} \mathcal{A}^B \mathcal{A}^C \quad (1.2)$$

⁴⁸ While many parallels can be drawn between Quantum Electrodynamics (QED, the theory that describes
⁴⁹ photons and electrons) and QCD, the difference between the two comes from the gluon-gluon interactions
⁵⁰ allowed in QCD, making it non-Abelian. These interactions can be summarized as shown in Figure 1.2.

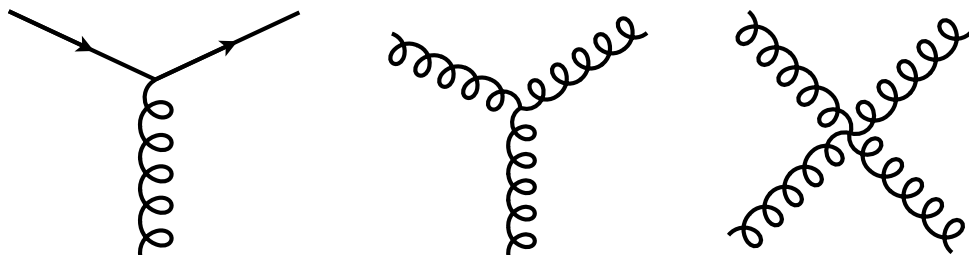


Figure 1.2: The allowed vertices in QCD. The vertices involving two or more gluons are unique to QCD and do not have a QED analog.

⁵¹ A core feature of QCD is that the coupling constant α_s has an energy dependence shown in Figure 1.3.
⁵² This dependence can be expressed in terms of the β function as

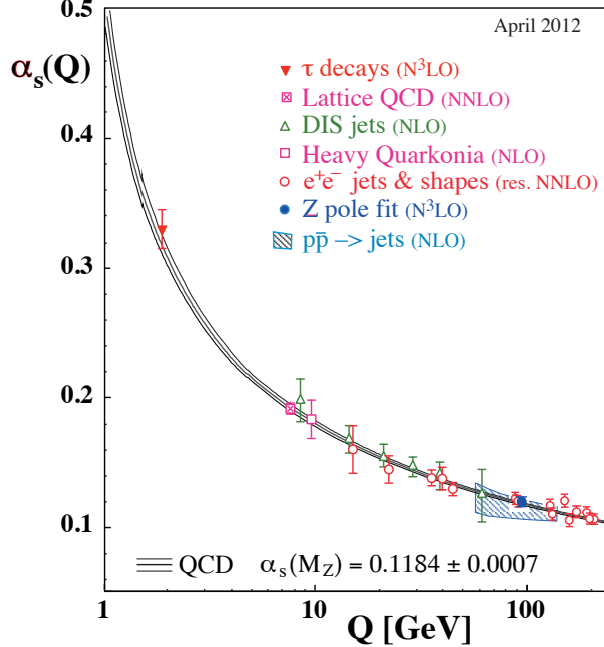


Figure 1.3: The running coupling constant α_s as a function of the momentum transfer Q . Figure taken from Ref. [2].

$$Q^2 \frac{\partial \alpha_s(Q^2)}{\partial Q^2} = \beta(\alpha_s(Q^2)) \quad (1.3)$$

53 where Q is the momentum transfer in the particle reaction. The beta function can be expressed using
 54 perturbative QCD (pQCD) as

$$\beta(\alpha_s) = -(b_0 \alpha_s^2 + b_1 \alpha_s^3 + b_2 \alpha_s^4 \dots) \quad (1.4)$$

55 where the coefficients b_i depend on the number of colors and flavors.

56 This running coupling constant is small and asymptotically tends to zero at large energy scales (or at
 57 small distances) and is large at small energy scales (large distances). This running coupling phenomenon
 58 leads to two key behaviors: asymptotic freedom and color confinement.

59 **Asymptotic Freedom:** At high energy scales (small distances), the QCD coupling constant α_s is
 60 small and tends to zero, implying a free particle behavior of quarks and gluons. This has been observed by a

61 variety of deep inelastic experiments [3–16]

62 **Color Confinement** The opposite end of the running coupling constant phenomenon is color confinement.
63 This property of QCD forbids the direct observation of free quarks and gluons, allowing only for
64 composite particles that are color singlets.

65 1.2 Heavy Ion Collisions

66 Heavy ion collisions can be used as a tool to study the Quark Gluon Plasma [17] . They provide access to
67 the otherwise confined partons, and give insight into the QCD phase diagram and the transition between the
68 QGP and hadronic matter.

69 In a heavy ion collision, the colliding nuclei are accelerated to relativistic energies and are Lorentz
70 contracted discs. In the case of a Pb+Pb collision the relativistic γ factor is between 100 and 2500 for
71 beam rapidities of $y = 5.3$ and 8.5 . Each nucleus contains many colored quarks and antiquarks, with three
72 more quarks than anti-quarks per nucleon, with the $q\bar{q}$ popping in and out of the vacuum due to quantum
73 fluctuations. These $q\bar{q}$ pairs are sources of transverse color fields and the corresponding force carriers, the
74 gluons.

75 When these pancake like discs collide, their color fields interact and there is a color charge exchange,
76 producing longitudinal color fields that fill the space between the receding discs. While the maximum energy
77 density in the process occurs just at the collision, the energy density 1 fm/c after the collision is 12 GeV/fm^3 ,
78 much higher than the 500 MeV/fm^3 in a typical hadron. Lattice QCD calculations in thermodynamics show
79 that at these energies, the partons produced in the collision cannot be treated as a collection of distinct
80 hadrons.

81 After the collision the energy density between the receding nuclei starts to decrease as the QGP cools and
82 expands. This process, seen in Figure 1.4, continues till the energy density drops to below that within a
83 hadron and the fluid “hadronizes”. These individual hadrons briefly scatter off of each other before they
84 freely fly towards the detector (freeze-out).

85 While Figure 1.4 shows snapshots of a head on (central) collision between two large nuclei, it is possible to
86 have collisions where the impact parameter is larger and hence the overlap region is smaller. These collisions,
87 called peripheral collisions, qualitatively undergo the same process described above, with the size and shape
88 of the QGP being different.

89 The basic parameters of a heavy ion collision such as the number of participants N_{part} and number of
90 binary collisions N_{coll} can be determined using the Glauber Monte Carlo simulations [19, 20]. This technique

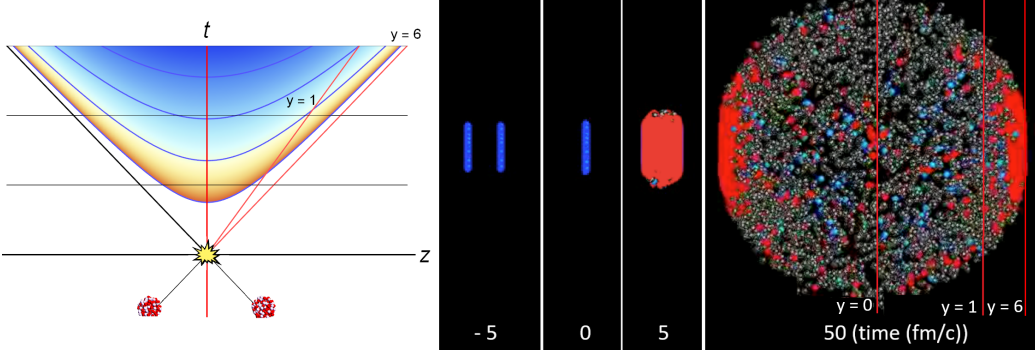


Figure 1.4: (left) Space-time diagram for a heavy ion collision. The color is indicative of the temperature of the QGP formed. (right) Snapshots of a heavy ion collision at $\sqrt{s_{NN}} = 2.76$ TeV at different times. The Lorentz contracted nuclei are in blue while the QGP is in red. Figure from Reference [18].

91 considers a nucleus-nucleus collision as a collection of independent binary nucleon-nucleon collisions; the
 92 colliding nuclei are modeled as a set of uncorrelated nucleons being positioned within the nucleus based on a
 93 the nuclear density function uniform in azimuthal and in polar angles. The nuclear density function shown in
 94 Figure 1.5 for Au and Cu, is given by:

$$\rho(r) = \rho_0 \frac{1 + w(r/R)^2}{1 + e^{\frac{r-R}{a}}} \quad (1.5)$$

95 where ρ_0 is the nucleon density, R is the nuclear radius, a is the skin depth, w corresponds to deviations
 96 from a circular shape and is typically zero for larger nuclei like Cu, W, Au, Pb, and U. For the Pb nuclei
 97 used at the LHC, $w = 0$, $R = 6.62$ fm and $a = 0.55$ fm [21].

98 They are then arranged with a random impact parameter b based on the distribution $d\sigma/db = 2\pi b$ and
 99 projected onto the $x - y$ plane as shown in Figure 1.6. They are then made to travel on straight trajectories,
 100 colliding if $d \leq \sqrt{\sigma_{\text{inel}}^{\text{NN}}/\pi}$, where d is the distance between the nucleons in a plane transverse to the beam
 101 axis and $\sigma_{\text{inel}}^{\text{NN}}$ is the inelastic scattering cross section. [22, 23]

102 An important parameter for colliding nuclei A and B with A and B nucleons is the thickness function
 103 T_{AB} . It describes the effective overlap area in which specific nucleons in the two colliding nuclei can interact.
 104 It can be defined in terms of the probability per unit area of a given nucleon being located at a particular
 105 distance s within the nucleus. For the colliding nuclei A and B , this is given by $T_A(\mathbf{s}) = \int \rho_A(\mathbf{s}, z_A) dz_A$ and
 106 $T_B(\mathbf{s}) = \int \rho_B(\mathbf{s}, z_B) dz_B$. Then, T_{AB} is given by

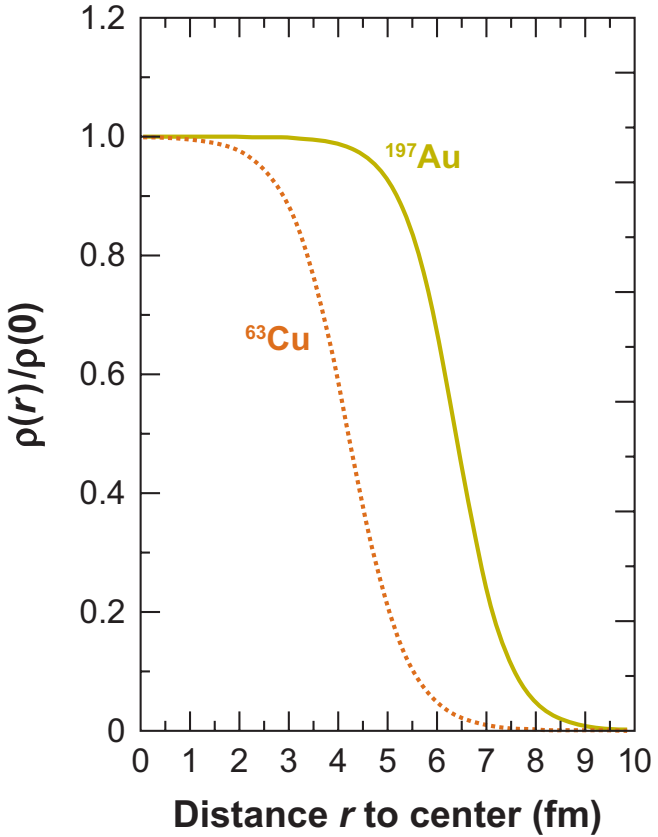


Figure 1.5: The nuclear density distributions for nuclei used at RHIC: Cu ($w = 0$, $R = 4.2$ fm and $a = 0.48$ fm) and Au ($w = 0$, $R = 6.38$ fm and $a = 0.535$ fm) [21, 22].

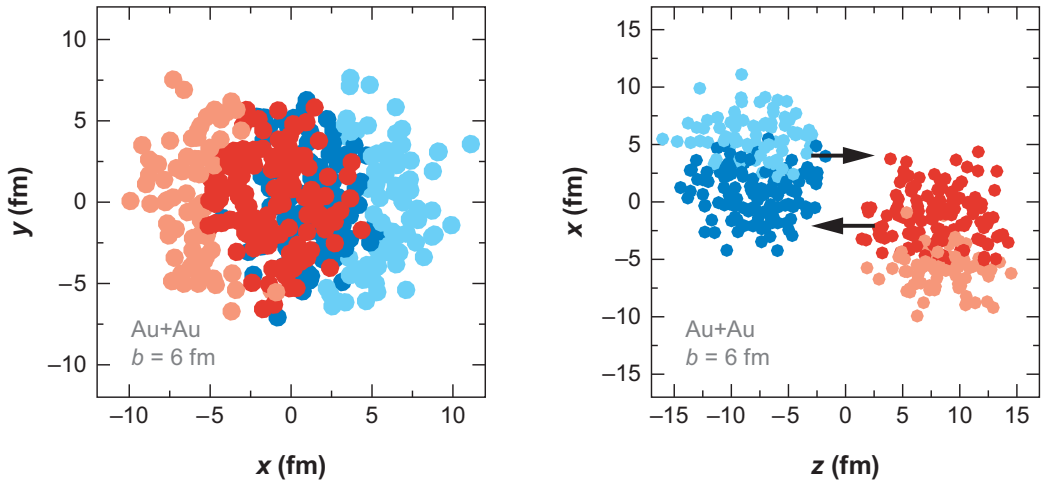


Figure 1.6: A Glauber Monte Carlo event for $Au + Au$ at $\sqrt{s_{NN}} = 200$ GeV with impact parameter of 6 fm viewed in the (left) transverse plane and (right) along the beam axis. Darker circles represent the participating nucleons. Taken from [22].

$$T_{AB}(\mathbf{b}) = \int T_A(\mathbf{s})T_B(\mathbf{s} - \mathbf{b})d^2s \quad (1.6)$$

107 The probability of then having n interactions between nuclei A and B is given by the binomial distribution:

$$P(n, \mathbf{b}) = \binom{AB}{n} \left[T_{AB}(\mathbf{b})\sigma_{\text{inel}}^{\text{NN}} \right]^n \left[1 - T_{AB}(\mathbf{b})\sigma_{\text{inel}}^{\text{NN}} \right]^{AB-n} \quad (1.7)$$

108 where the first term is the number of combinations for finding n collisions from AB possibilities, the
 109 second term is the probability for having exactly n collisions, and the last term the probability of $AB - n$
 110 misses. Then the total probability of an interaction between A and B is

$$\frac{d^2\sigma_{\text{inel}}^{\text{AB}}}{db^2} \equiv p_{\text{inel}}^{\text{AB}}(b) = \sum_{n=1}^{AB} P(n, \mathbf{b}) = 1 - \left[1 - T_{AB}(\mathbf{b})\sigma_{\text{inel}}^{\text{NN}} \right]^{AB} \quad (1.8)$$

111 Then the total cross section is given by

$$\sigma_{\text{inel}}^{\text{AB}} = \int_0^\infty 2\pi b db \left[1 - \left(1 - T_{AB}(\mathbf{b})\sigma_{\text{inel}}^{\text{NN}} \right)^{AB} \right] \quad (1.9)$$

112 and N_{coll} and N_{part} are given by [24, 25]

$$N_{\text{coll}}(b) = \sum_{n=1}^{AB} n P(n, b) = AB \times T_{AB}(b)\sigma_{\text{inel}}^{\text{NN}} \quad (1.10)$$

$$N_{\text{part}}(b) = A \int T_A(\mathbf{s}) \left[1 - \left(1 - T_B(\mathbf{s} - \mathbf{b})\sigma_{\text{inel}}^{\text{NN}} \right)^B \right] d^2s + B \int T_B(\mathbf{s} - \mathbf{b}) \left[1 - \left(1 - T_A(\mathbf{s})\sigma_{\text{inel}}^{\text{NN}} \right)^A \right] d^2s \quad (1.11)$$

113 The correlation between N_{coll} and N_{part} can be seen in Figure 1.7

114 The charged particle multiplicity N_{ch} along with the combination of N_{part} and impact parameter b can
 115 be used to determine the centrality of a heavy ion event. An example of this is shown in Figure 1.8.

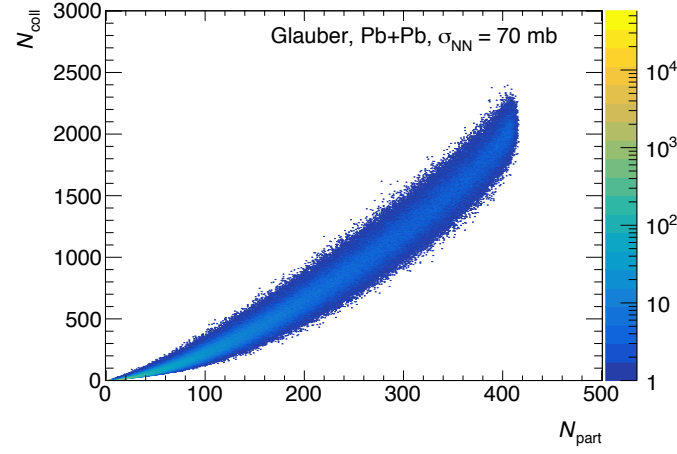


Figure 1.7: The $N_{\text{coll}} - N_{\text{part}}$ correlation for Pb+Pb collisions at $\sqrt{s_{\text{NN}}} = 5.02 \text{ TeV}$. Taken from [26].

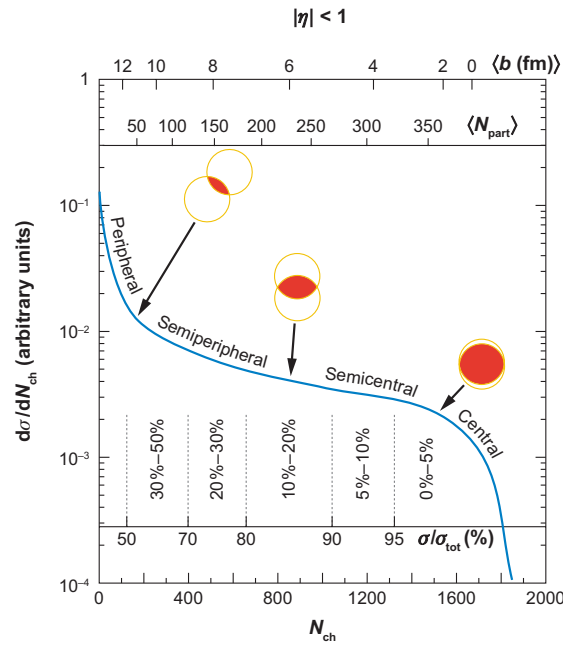


Figure 1.8: The correlation between the observable N_{ch} and N_{part} to determine the centrality distribution. Taken from [22].

116 1.3 Quark Gluon Plasma

117 Extreme conditions of temperature and pressure like those in relativistic heavy ion collisions lead to the
 118 formation of the Quark Gluon Plasma [17]. It is believed to have filled the early universe a few microseconds
 119 after the Big Bang and might be present in the cores of extremely compact objects like neutron stars [27,
 120 28]. The phase transition between the free quarks and gluons within the QGP and the confined quarks and
 121 gluons within hadrons can be seen in Figure 1.9.

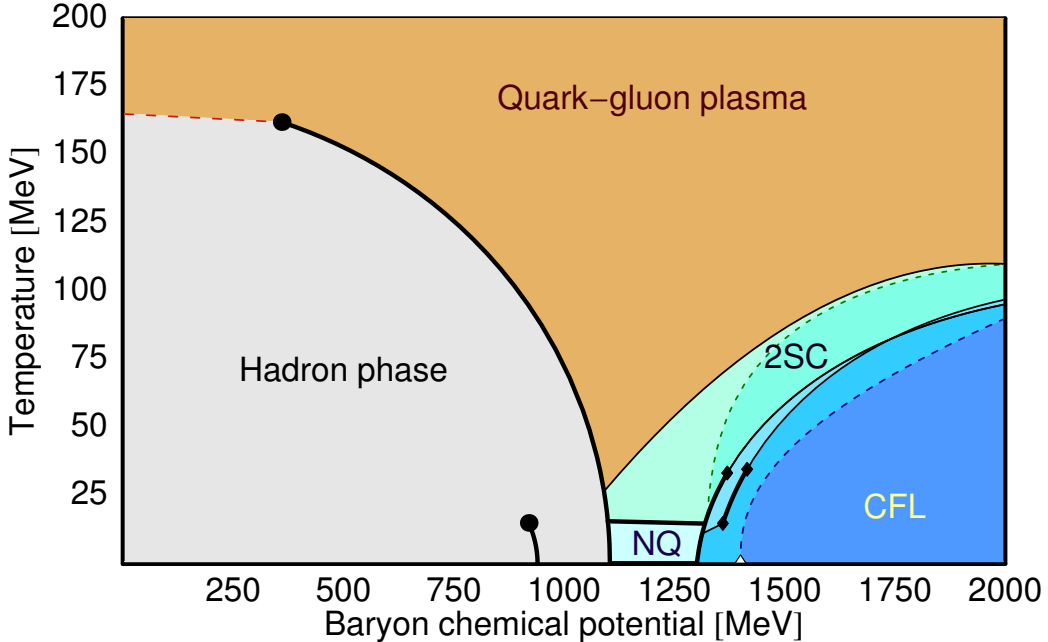


Figure 1.9: The QCD phase diagram of nuclear matter. Figure from Reference [29].

122 This state of matter exists for 1–10 fm/c, depending on the collision energy, above $\lambda_{\text{QCD}} = 200$ MeV, the
 123 fundamental energy scale in QCD. Thermal photons from the QGP reveal that it reaches temperatures of
 124 300–600 MeV in central collisions at 200 GeV [30] and 2.76 TeV [31], showing very little collision energy
 125 dependence. Further, the chemical freeze-out temperature was found to be 160 MeV via measurements of
 126 ratios of final state hadrons containing the light u, d quarks [32–34] with the thermal freeze-out being 100–150
 127 MeV [35–38]. These measurements paint a picture of the QGP being formed early in the heavy ion collision.
 128 It has a non-uniform energy density and temperature determined by the 'colliding nuclei and collision energy.
 129 The QGP then cools and expands as described by relativistic hydrodynamics, and as its temperature falls
 130 below 160 MeV, it experiences a crossover phase transition and hadronizes. This system continues to cool
 131 and expand, until at 95 GeV there is a thermal freeze-out.

132 The QGP was initially thought to be a weakly coupled parton gas because of asymptotic freedom from

133 QCD. The highly energetic collisions such as those at the LHC would imply a weak interaction between the
 134 quarks and gluons that make up the plasma. This would result in rare scatterings between the constituents
 135 of the gas and wash out any spatial anisotropies based on the collision geometry. On the other hand, a
 136 strong coupling within the QGP would result in the pressure gradients in the medium being driven by
 137 hydrodynamics and spatial anisotropies would be transformed to momentum anisotropies in the particles
 138 produced as shown in Figure 1.10. In this picture, the non-uniform structure of the colliding nuclei would
 139 cause a momentum anisotropy that would be further enhanced when looking at collisions that are less central
 140 and do not have perfect overlap between the colliding nuclei. These observations were seen in azimuthal
 141 correlation measurements implying that the medium is indeed strongly coupled [39–42].

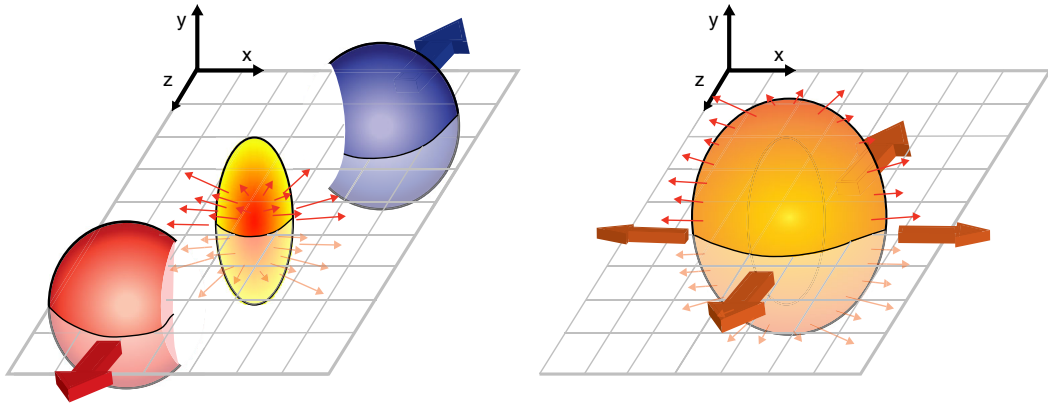


Figure 1.10: Schematic diagrams of the initial overlap region (left) and the final spatial anisotropy generated (right). Taken from [43].

142 A Fourier Transform of the angular distribution of charged hadrons in the collision debris can quantify
 143 these momentum anisotropies and give the anisotropic flow coefficients v_n , defined as [44]:

$$\frac{d\bar{N}}{d\phi} = \frac{\bar{N}}{2\pi} \left(1 + 2 \sum_{n=1}^{\infty} v_n \cos(n(\phi - \bar{\Psi}_n)) \right) \quad (1.12)$$

144 where ϕ is the angle in the transverse plane, $\bar{\Psi}_n$ are the event plane angles, and \bar{N} is the average number
 145 of particles per event. Some of these coefficients are shown in Figure 1.11. The measured anisotropies can be
 146 used to constrain the specific viscosity given by the ratio of viscosity to entropy density, η/s , and have shown
 147 that the QGP has a η/s of near the theoretical minimum of $1/4\pi$ [45].

148 The Bjorken energy density of the QGP can be derived using [48]:

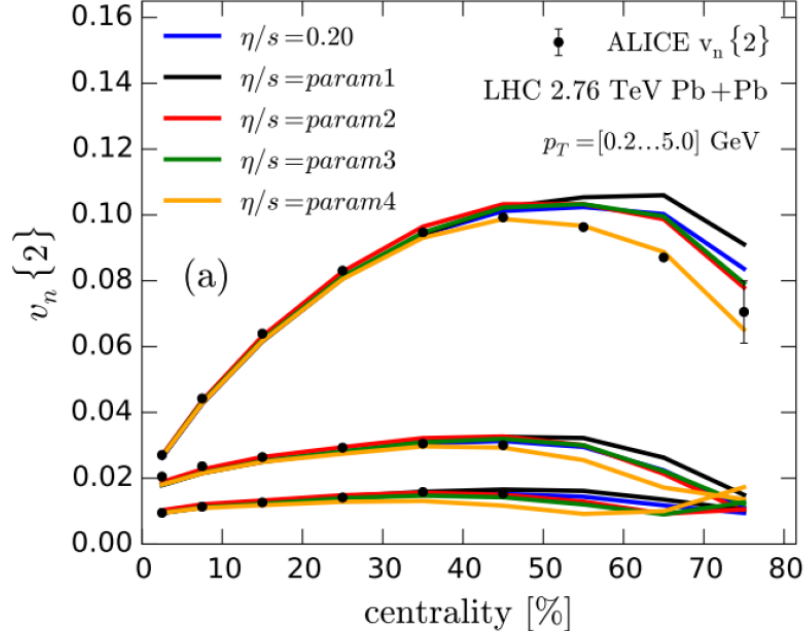


Figure 1.11: Comparison of a hydrodynamic model from [46] to anisotropy measurements by ALICE [47] for different parameterizations of η/s and for different v_n , $n = 2, 3, 4$ from top to bottom, as a function of collision centrality.

$$\varepsilon \geq \frac{dE_T/d\eta}{\tau_0 \pi R^2} = \frac{3}{2} \langle E_T/N \rangle \frac{dN_{ch}/d\eta}{\tau_0 \pi R^2} \quad (1.13)$$

where $dN_{ch}/d\eta$ is the number of charged particles produced per unity pseudorapidity, $dE_T/d\eta$ is the transverse energy per unit pseudorapidity, τ_0 is the thermalization time, R is the nuclear radius, and $E_T/N \approx 1$ GeV is the transverse energy per emitted particle. As shown in Figure 1.12, the energy density at the LHC was measured to be approximately 15 GeV/fm 3 , much higher than the values measured at RHIC [49, 50].

1.4 Jets and Jet Quenching

Hard scatterings in particle collisions result in the production of highly energetic partons that form conical sprays of hadrons called jets. A schematic of this process is shown in Figure 1.13. Jet production in a vacuum is well described in context of perturbative QCD [52] where processes involving large momentum transfers like high p_T hadron production can be described in terms of the parton distribution functions, scattering cross sections, and final state fragmentation functions as shown below [53]:

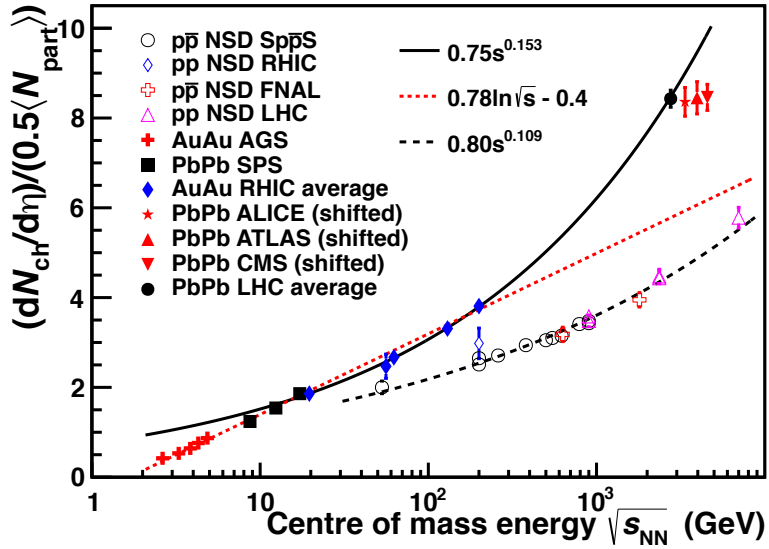


Figure 1.12: $dN_{\text{ch}}/d\eta$ per colliding nucleon pair as a function of collision energy in pp and nucleus-nucleus collisions [51].

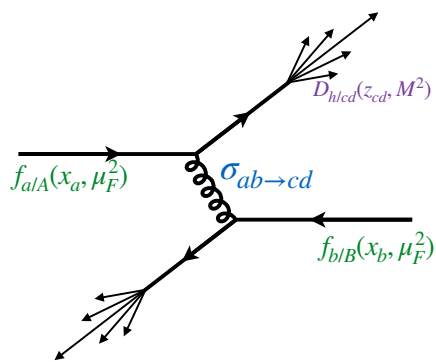


Figure 1.13: Jet production from the process $pp \rightarrow hX$, factorizing in terms of the parton distribution functions, scattering cross sections, and jet fragmentation functions. [53]

$$\begin{aligned}
d\sigma_{pp \rightarrow hX} \approx & \sum_{abjd} \int dx_a \int dx_b \int dz_j f_{a/p}(x_a, \mu_f) \otimes f_{b/p}(x_b, \mu_f) \\
& \otimes d\sigma_{ab \rightarrow jd}(\mu_f, \mu_F, \mu_R) \\
& \otimes D_{j \rightarrow h}(z_j, \mu_f)
\end{aligned} \tag{1.14}$$

159 where $x_a = p_a/P_A, x_b = p_b/P_b$ are the initial momentum fractions carried by the interacting partons,
 160 $z_j = p_h/p_j$ is the momentum fraction carried by the final observed hadron. $f_{a/p}(x_a, \mu_f)$ and $f_{b/p}(x_b, \mu_f)$ are
 161 the two parton distribution functions (PDFs), $d\sigma_{ab \rightarrow jd}(\mu_f, \mu_F, \mu_R)$ is the differential cross section for parton
 162 scattering and $D_{j \rightarrow h}(z_j, \mu_f)$ is the fragmentation function (FFs) for parton j to hadron h . μ_f and μ_F are the
 163 factorization scales and μ_R is the renormalization scale, and are typically taken to be the same hard scale Q .
 164 The PDFs characterize the initial state and represent the probability of finding a parton with momentum
 165 fraction x (shown in Figure 1.14) in the initial hadron, while the FFs describe the probability of fragmenting
 166 to a hadron h with given kinematic properties.

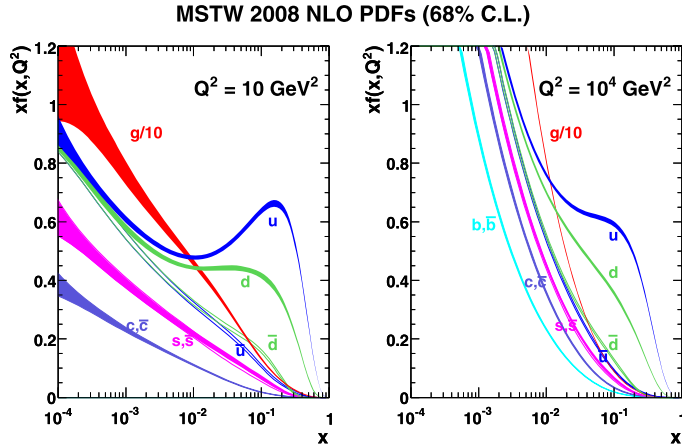


Figure 1.14: The next to leading order (NLO) PDFs at (left) $Q^2 = 10 \text{ GeV}^2$ and (right) $Q^2 = 10^4 \text{ GeV}^2$. The band is the associated one-sigma (68%) confidence level uncertainty. Taken from [54]

167 In the case of heavy ion collisions, the jet observables can be modified due to two sources: the nuclear
 168 PDF being distinct from a proton PDF, and the formation of the quark gluon plasma.
 169 The former is collectively referred to as cold nuclear matter (CNM) effect, and can be quantified by
 170 defining a nuclear modification factor for the PDF:

$$R_a^A(x, Q^2) = \frac{f_{a/A}(x, Q^2)}{f_{a/p}(x, Q^2)} \quad (1.15)$$

where $f_{a/A}$ and $f_{a/p}$ are the nuclear and proton PDFs respectively. This R_a^A factor is determined by global fits to data from DIS measurements [55–57]. CNM effects include the following contributions:

- Shadowing: This is a destructive interference effect that reduces the interactions of a nucleon incident on a nucleus within its interior and on its back face. This effect reduces the effective number of nucleons in an inelastic interaction to $A^{2/3}$. For Q^2 of the order of a few GeV^2 , this effect dominates for $x < 0.05$ and implies $R_a^A(x, Q^2) < 1$ [58].
- Anti-shadowing: This compensates for the shadowing effect based on the momentum sum rule, and for Q^2 of the order of a few GeV^2 implies $R_a^A(x, Q^2) > 1$ over the region $0.05 < x < 0.20$.
- EMC: The modification of the nuclear structure function was first observed by the European Muon Collaboration [59]. Recent observations have suggested that the effect is caused by short-range correlated nucleon pairs within nuclei [60]. For Q^2 of the order of a few GeV^2 , this effect dominates for $0.2 < x < 0.80$ and implies $R_a^A(x, Q^2) < 1$.
- Fermi Motion: This effect considers the motion of the nucleons within the nucleus. It results in $R_a^A(x, Q^2) > 1$ over the $x > 0.8$ region for Q^2 of the order of a few GeV^2 [61].

Cold nuclear matter effects are experimentally measured using $p + A$ systems where the size and shape of the plasma, and hence any effects thereof, are a lot smaller.

The second source of modification is the formation of the hot and dense quark gluon plasma. The hot nuclear matter effects further serve as an independent confirmation that the medium formed is strongly interacting. Jets are formed early enough that they traverse the Quark Gluon Plasma and as strongly interacting particles, are both affected by, and affect the QGP. This interaction typically results in the jet losing energy and forward momentum [62, 63], with the lost energy being deposited in the medium [64]. Jets can also pick up momentum transverse to the parton direction [65]. The hot nuclear matter effects can be considered to be a combination of collisional and radiative energy losses summarized in Figure 1.15.

- Collisional energy loss: This is a combination of elastic and inelastic collisions of the hard parton with the constituents of the quark gluon plasma.
- Radiative energy loss: This is the larger source of parton energy loss and jet quenching. These are modified by the presence of the plasma due to scatterings off of the plasma constituents. A variety of

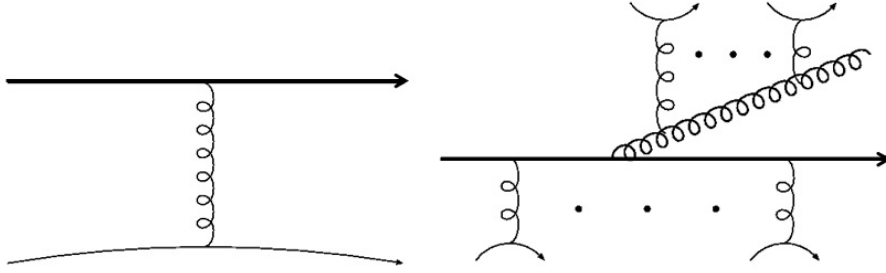


Figure 1.15: The typical diagrams for (left) collisional and (right) radiative energy losses for a parton in a hard scattering as it propagates through the QGP. Taken from [53]

198 radiative energy loss frameworks that have been developed include: Baier-Dokshitzer-Mueller-Peigne-
 199 Schiff-Zakharov (BDMPS-Z) [66], Gyulassy, Levai and Vitev (GLV) [67], Amesto-Salgado-Wiedemann
 200 (ASW) [68], Arnold-Moore-Yaffe (AMY) [69] and higher twist (HT) [70].

201 **Collisional energy loss** This is a combination of elastic and inelastic collisions of the hard parton
 202 with the constituents of the quark gluon plasma. The

Both hot and cold nuclear matter effects can be described by modifying Equation 1.14 as:

$$d\sigma_{AB \rightarrow hX} \approx \sum_{abjj'd} f_{a/A}(x_a) \otimes f_{b/B}(x_b) \otimes d\sigma_{ab \rightarrow jd}(\mu_f, \mu_F, \mu_R) \otimes P_{j \rightarrow j'} \otimes D_{h \rightarrow j'}(z_j, \mu_f) \quad (1.16)$$

203 where the additional $P_{j \rightarrow j'}$ describes the interaction of the hard parton with the colored medium. This is
 204 typically taken as part of the fragmentation modification as:

$$\tilde{D}_{h \rightarrow j'}(z_j, \mu_f) \approx \sum_{j'} P_{j \rightarrow j'}(p_{j'}|p_j) \otimes D_{h \rightarrow j'}(j') \quad (1.17)$$

205 1.4.1 Jet Reconstruction

206 Jets can be reconstructed by clustering algorithms that take in a variety of inputs. The algorithm used in
 207 ATLAS is the anti- k_t clustering algorithm [71]. This algorithm clusters soft particles around hard ones in the
 208 following manner:

- 209 • Calculate all distances d_{ij} between entities i and j , and distance d_{iB} between entity i and beam B .
- 210 • Identify the smallest distances such that for the smallest distance d_{ij} , the entities i and j are combined
211 and return to beginning.
- 212 • If the smallest distance is d_{iB} , then take i as the jet and remove it from the list of entities and return
213 to beginning.
- 214 • Continue the procedure till the list of items is empty.

215 In general the distance d_{ij} between the objects is found the via the prescription

$$d_{ij} = \min(k_{Ti}^{2p}, k_{Tj}^{2p}) \frac{\Delta_{ij}^2}{R^2} \quad (1.18)$$

$$d_{iB} = k_{Ti}^{2p} \quad (1.19)$$

216 where k_{Ti} is the transverse momentum of particle i and $\Delta_{ij} = \sqrt{\Delta\eta_{ij}^2 + \Delta\phi_{ij}^2}$ is the distance between
217 particles i and j in $\eta-\phi$ space. R the distance parameter and reflects the size of the jet being considered. In the
218 case of the anti- k_t algorithm, $p = -1$. Other popular clustering algorithms like k_t [72] and Cambridge/Aachen
219 [73] use $p = 1$ and $p = 0$ respectively. The behavior of the different clustering algorithms is shown in
220 Figure 1.16.

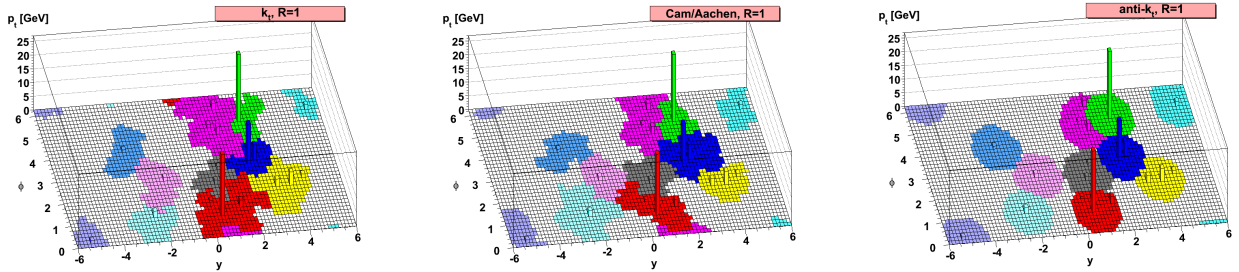


Figure 1.16: Different clustering algorithms applied to the sample parton-level event. Figure taken from [71].

221 The popularity of the anti- k_t algorithm comes from its overcoming of two common problems: collinear
222 and infrared safety. These are related to instabilities in the cones that are found due to soft radiation.

223 Figure 1.17 describes the collinear safety problem. In a collinear safe jet algorithm, the presence of a virtual
224 loop or a collinear splitting of a central particle would not change the number of jets being reconstructed.
225 On the other hand, while a collinear unsafe jet algorithm would not change its output with the presence
226 of a virtual loop, a splitting in the central particle would lead to the left and right most particles forming
227 individual seeds, implying two reconstructed jets [74].

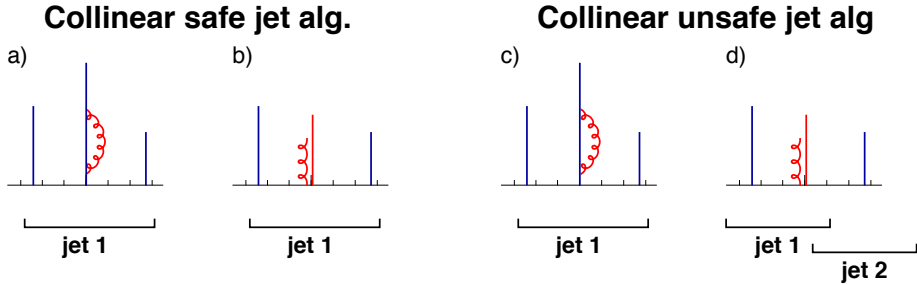


Figure 1.17: An illustration of collinear unsafe behavior. The particle p_T is proportional to the height and the horizontal axis indicates rapidity. Taken from [74].

228 A schematic describing infrared un-safety is shown in Figure 1.18. Here an infrared safe algorithm would
 229 use the three particles as seeds iteratively find two stable cones. An unsafe algorithm however would find
 230 three overlapping cones based on the addition of a soft seed.

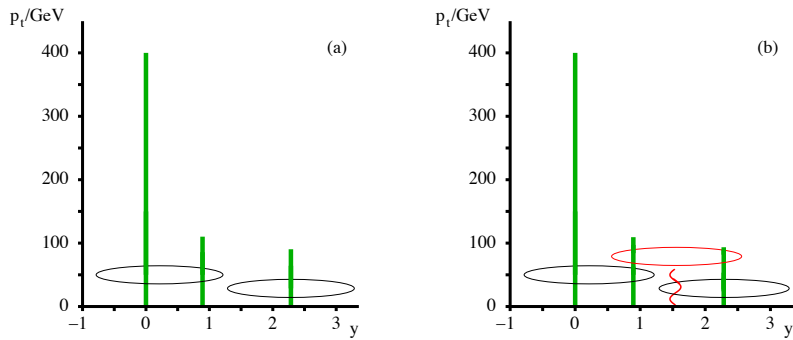


Figure 1.18: An illustration of infrared unsafe behavior. The particle p_T is proportional to the height and the horizontal axis indicates rapidity. Taken from [75]

231 For heavy ion collisions in ATLAS, the inputs to the algorithm are the $\eta \times \phi = 0.1 \times 0.1$ calorimeter
 232 towers. The tower energies are determined by summing up the energies of the individual calorimeter cells.
 233 The anti- k_t algorithm is first run with the distance parameter $R = 0.2$, following which an underlying event
 234 subtraction procedure is performed. A first estimate of the average underlying event energy density $\rho_i(\eta)$ is
 235 done in 0.1 slices of η in each calorimeter layer i after excluding the regions that overlap with the seed jets.
 236 A modulation of $2v_2 \cos[2(\phi - \Psi_2)]$ is applied to account for the flow from the QGP and the underlying event
 237 is subtracted to give E_{Tj}^{sub} :

$$E_{Tj}^{\text{sub}} = E_{Tj} - A_j \rho_i(\eta_j) 1 + 2v_{2i} (\cos[2(\phi - \Psi_2)]) \quad (1.20)$$

238 where E_{Tj}, η_j, ϕ_j and A_j are the cell E_T, η, ϕ and area for cell j in layer i . This process is done iteratively

239 done one more time after getting new seeds with the distance parameter $R = 0.2$ and excluding areas that
240 are within $\Delta R = 0.4$ of the seeds. Updated values of ρ'_i and v'_2 are recalculated and used to estimate the
241 background that is subtracted from the original cell energies. More details on this procedure can be found in
242 [76].

Chapter 2

Major Jet Measurements

²⁴³ This chapter shall discuss some important experimental jet measurements that motivate the study of the
²⁴⁴ main analysis in this thesis. It will begin with a brief discussion of the jet reconstruction procedure and go
²⁴⁵ on to discuss measurements of jet yields, dijet asymmetry, and jet fragmentation.

²⁴⁶ 2.1 Modification of jet yields: Jet R_{AA}

²⁴⁷ Jet R_{AA} and Jet R_{AA}

²⁴⁸ 2.2 Jet X_J

²⁴⁹ 2.3 Jet Fragmentation

Bibliography

- [1] M. K. Gaillard, P. D. Grannis and F. J. Sciulli, *The Standard model of particle physics*, Rev. Mod. Phys. **71** (1999) S96, arXiv: [hep-ph/9812285 \[hep-ph\]](#) (cit. on p. 1).
- [2] J Beringer et al., *Review of Particle Physics, 2012-2013. Review of Particle Properties*, Phys. Rev. D **86** (2012) 010001 (cit. on pp. 2, 3).
- [3] A. Deur et al., *High precision determination of the Q^2 evolution of the Bjorken Sum*, Phys. Rev. **D90** (2014) 012009, arXiv: [1405.7854 \[nucl-ex\]](#) (cit. on p. 4).
- [4] J. H. Kim et al., *A Measurement of $\alpha_s(Q^2)$ from the Gross-Llewellyn Smith sum rule*, Phys. Rev. Lett. **81** (1998) 3595, arXiv: [hep-ex/9808015 \[hep-ex\]](#) (cit. on p. 4).
- [5] G. Altarelli et al., *Determination of the Bjorken sum and strong coupling from polarized structure functions*, Nucl. Phys. **B496** (1997) 337, arXiv: [hep-ph/9701289 \[hep-ph\]](#) (cit. on p. 4).
- [6] H. W. Kendall, *Deep inelastic scattering: Experiments on the proton and the observation of scaling*, Rev. Mod. Phys. **63** (3 1991) 597 (cit. on p. 4).
- [7] A. L. Kataev, G. Parente and A. V. Sidorov, *Improved fits to the xF_3 CCFR data at the next-to-next-to-leading order and beyond*, Phys. Part. Nucl. **34** (2003) 20, [Erratum: Phys. Part. Nucl.38,no.6,827(2007)], arXiv: [hep-ph/0106221 \[hep-ph\]](#) (cit. on p. 4).
- [8] S. Alekhin, J. Blumlein and S. Moch, *Parton Distribution Functions and Benchmark Cross Sections at NNLO*, Phys. Rev. **D86** (2012) 054009, arXiv: [1202.2281 \[hep-ph\]](#) (cit. on p. 4).
- [9] S. Alekhin, J. Blumlein and S.-O. Moch, *ABM news and benchmarks*, PoS **DIS2013** (2013) 039, arXiv: [1308.5166 \[hep-ph\]](#) (cit. on p. 4).
- [10] J. Blumlein, H. Bottcher and A. Guffanti, *Non-singlet QCD analysis of deep inelastic world data at $O(\alpha_s^3)$* , Nucl. Phys. **B774** (2007) 182, arXiv: [hep-ph/0607200 \[hep-ph\]](#) (cit. on p. 4).
- [11] H1 Collaboration, *Three- and Four-jet Production at Low x at HERA*, Eur. Phys. J. **C54** (2008) 389, arXiv: [0711.2606 \[hep-ex\]](#) (cit. on p. 4).

- 273 [12] ZEUS Collaboration, *Forward-jet production in deep inelastic ep scattering at HERA*, Eur. Phys. J.
 274 **C52** (2007) 515, arXiv: [0707.3093 \[hep-ex\]](#) (cit. on p. 4).
- 275 [13] ZEUS Collaboration, *Multi-jet cross-sections in charged current $e^\pm p$ scattering at HERA*, Phys. Rev.
 276 **D78** (2008) 032004, arXiv: [0802.3955 \[hep-ex\]](#) (cit. on p. 4).
- 277 [14] ZEUS Collaboration, *Inclusive dijet cross sections in neutral current deep inelastic scattering at HERA*,
 278 Eur. Phys. J. **C70** (2010) 965, arXiv: [1010.6167 \[hep-ex\]](#) (cit. on p. 4).
- 279 [15] ZEUS Collaboration, *Inclusive-jet cross sections in NC DIS at HERA and a comparison of the kT ,*
 280 *anti- kT and SIScone jet algorithms*, Phys. Lett. **B691** (2010) 127, arXiv: [1003.2923 \[hep-ex\]](#) (cit. on
 281 p. 4).
- 282 [16] H1 Collaboration, *Jet Production in ep Collisions at High Q^2 and Determination of α_s* , Eur. Phys. J.
 283 **C65** (2010) 363, arXiv: [0904.3870 \[hep-ex\]](#) (cit. on p. 4).
- 284 [17] E. V. Shuryak, *Quantum chromodynamics and the theory of superdense matter*, Physics Reports **61**
 285 (1980) 71, ISSN: 0370-1573 (cit. on pp. 4, 9).
- 286 [18] W. Busza et al., *Heavy Ion Collisions: The Big Picture, and the Big Questions*, Ann. Rev. Nucl. Part.
 287 Sci. **68** (2018) 339, arXiv: [1802.04801 \[hep-ph\]](#) (cit. on p. 5).
- 288 [19] R. Glauber, *Lectures in theoretical physics*, ed. WE Brittin and LG Dunham, Interscience, New York **1**
 289 (1959) 315 (cit. on p. 4).
- 290 [20] R. Glauber et al., *Lectures in theoretical physics*, 1959 (cit. on p. 4).
- 291 [21] H. D. Vries, C. D. Jager and C. D. Vries, *Nuclear charge-density-distribution parameters from elastic*
 292 *electron scattering*, Atomic Data and Nuclear Data Tables **36** (1987) 495, ISSN: 0092-640X (cit. on pp. 5,
 293 6).
- 294 [22] M. L. Miller, K. Reygers, S. J. Sanders and P. Steinberg, *Glauber Modeling in High-Energy Nuclear*
 295 *Collisions*, Annual Review of Nuclear and Particle Science **57** (2007) 205, eprint: <https://doi.org/10.1146/annurev.nucl.57.090506.123020> (cit. on pp. 5, 6, 8).
- 297 [23] B. Alver, M. Baker, C. Loizides and P. Steinberg, *The PHOBOS Glauber Monte Carlo*, (2008), arXiv:
 298 [0805.4411 \[nucl-ex\]](#) (cit. on p. 5).
- 299 [24] D. Kharzeev and M. Nardi, *Hadron production in nuclear collisions at RHIC and high density QCD*,
 300 Phys. Lett. **B507** (2001) 121, arXiv: [nucl-th/0012025 \[nucl-th\]](#) (cit. on p. 7).
- 301 [25] A. Bialas, M. Bleszynski and W. Czyz, *Multiplicity Distributions in Nucleus-Nucleus Collisions at*
 302 *High-Energies*, Nucl. Phys. **B111** (1976) 461 (cit. on p. 7).

- 303 [26] ATLAS Collaboration, *Centrality determination in $\sqrt{s_{NN}} = 5.02$ TeV Pb+Pb collision data in 2015*,
 304 tech. rep. ATL-COM-PHYS-2016-1287, CERN, 2016 (cit. on p. 8).
- 305 [27] J. C. Collins and M. J. Perry, *Superdense Matter: Neutrons or Asymptotically Free Quarks?*, Phys. Rev.
 306 Lett. **34** (21 1975) 1353 (cit. on p. 9).
- 307 [28] A. D. Linde, *Phase transitions in gauge theories and cosmology*, Reports on Progress in Physics **42**
 308 (1979) 389 (cit. on p. 9).
- 309 [29] S. B. Ruster, V. Werth, M. Buballa, I. A. Shovkovy and D. H. Rischke, *Phase diagram of neutral quark
 310 matter: Self-consistent treatment of quark masses*, Phys. Rev. D **72** (3 2005) 034004 (cit. on p. 9).
- 311 [30] PHENIX Collaboration, *Enhanced Production of Direct Photons in Au + Au Collisions at $\sqrt{s_{NN}} =$
 312 200 GeV and Implications for the Initial Temperature*, Phys. Rev. Lett. **104** (13 2010) 132301 (cit. on
 313 p. 9).
- 314 [31] ALICE Collaboration, *Direct photon production in Pb–Pb collisions at sNN=2.76 TeV*, Physics Letters
 315 B **754** (2016) 235, ISSN: 0370-2693 (cit. on p. 9).
- 316 [32] Z. Fodor and S. Katz, *Critical point of QCD at finite T and λ , lattice results for physical quark masses*,
 317 Journal of High Energy Physics **2004** (2004) 050 (cit. on p. 9).
- 318 [33] STAR Collaboration, *Experimental and theoretical challenges in the search for the quark-gluon plasma:
 319 The STAR Collaboration's critical assessment of the evidence from RHIC collisions*, Nuclear Physics A
 320 **757** (2005) 102, First Three Years of Operation of RHIC, ISSN: 0375-9474 (cit. on p. 9).
- 321 [34] ALICE Collaboration, *Production of light nuclei and anti-nuclei in pp and Pb-Pb collisions at energies
 322 available at the CERN Large Hadron Collider*, Phys. Rev. C **93** (2 2016) 024917 (cit. on p. 9).
- 323 [35] PHENIX Collaboration, *Single identified hadron spectra from $\sqrt{s_{NN}} = 130$ GeV Au + Au collisions*,
 324 Phys. Rev. C **69** (2 2004) 024904 (cit. on p. 9).
- 325 [36] BRAHMS Collaboration, *Centrality dependent particle production at $y = 0$ and $y \geq 1$ in Au+Au collisions
 326 at $\sqrt{s_{NN}} = 200$ GeV*, Phys. Rev. C **72** (1 2005) 014908 (cit. on p. 9).
- 327 [37] PHOBOS Collaboration, *Identified hadron transverse momentum spectra in Au+Au collisions at
 328 $\sqrt{s_{NN}} = 62.4$ GeV*, Phys. Rev. C **75** (2 2007) 024910 (cit. on p. 9).
- 329 [38] ALICE Collaboration, *Centrality dependence of π , K, and p production in Pb-Pb collisions at $\sqrt{s_{NN}} =$
 330 2.76 TeV*, Phys. Rev. C **88** (4 2013) 044910 (cit. on p. 9).

- 331 [39] ATLAS Collaboration, *Measurement of the azimuthal anisotropy of charged particles produced in $\sqrt{s_{NN}} =$*
 332 *5.02 TeV Pb+Pb collisions with the ATLAS detector*, Eur. Phys. J. **C78** (2018) 997, arXiv: [1808.03951](#)
 333 [[nucl-ex](#)] (cit. on p. 10).
- 334 [40] PHENIX Collaboration, *Elliptic Flow of Identified Hadrons in Au + Au Collisions at $\sqrt{s_{NN}} = 200$*
 335 *GeV*, Phys. Rev. Lett. **91** (18 2003) 182301 (cit. on p. 10).
- 336 [41] CMS Collaboration, *Non-Gaussian elliptic-flow fluctuations in PbPb collisions at $\sqrt{s_{NN}} = 5.02$ TeV*,
 337 Phys. Lett. **B789** (2019) 643, arXiv: [1711.05594](#) [[nucl-ex](#)] (cit. on p. 10).
- 338 [42] ALICE Collaboration, *Anisotropic Flow of Charged Particles in Pb-Pb Collisions at $\sqrt{s_{NN}} = 5.02$ TeV*,
 339 Phys. Rev. Lett. **116** (13 2016) 132302 (cit. on p. 10).
- 340 [43] M. Connors, C. Nattrass, R. Reed and S. Salur, *Jet measurements in heavy ion physics*, Rev. Mod.
 341 Phys. **90** (2 2018) 025005 (cit. on p. 10).
- 342 [44] A. M. Poskanzer and S. A. Voloshin, *Methods for analyzing anisotropic flow in relativistic nuclear*
 343 *collisions*, Phys. Rev. **C58** (1998) 1671, arXiv: [nucl-ex/9805001](#) [[nucl-ex](#)] (cit. on p. 10).
- 344 [45] U. Heinz and R. Snellings, *Collective flow and viscosity in relativistic heavy-ion collisions*, Ann. Rev.
 345 Nucl. Part. Sci. **63** (2013) 123, arXiv: [1301.2826](#) [[nucl-th](#)] (cit. on p. 10).
- 346 [46] H. Niemi, K. J. Eskola and R. Paatelainen, *Event-by-event fluctuations in a perturbative QCD +*
 347 *saturation + hydrodynamics model: Determining QCD matter shear viscosity in ultrarelativistic heavy-*
 348 *ion collisions*, Phys. Rev. **C93** (2016) 024907, arXiv: [1505.02677](#) [[hep-ph](#)] (cit. on p. 11).
- 349 [47] ALICE Collaboration, *Higher harmonic anisotropic flow measurements of charged particles in Pb-Pb*
 350 *collisions at $\sqrt{s_{NN}} = 2.76$ TeV*, Phys. Rev. Lett. **107** (2011) 032301, arXiv: [1105.3865](#) [[nucl-ex](#)]
 351 (cit. on p. 11).
- 352 [48] J. D. Bjorken, *Highly relativistic nucleus-nucleus collisions: The central rapidity region*, Phys. Rev. D
 353 **27** (1 1983) 140 (cit. on p. 10).
- 354 [49] PHENIX Collaboration, *Formation of dense partonic matter in relativistic nucleus-nucleus collisions at*
 355 *RHIC: Experimental evaluation by the PHENIX collaboration*, Nucl. Phys. **A757** (2005) 184, arXiv:
 356 [nucl-ex/0410003](#) [[nucl-ex](#)] (cit. on p. 11).
- 357 [50] CMS Collaboration, *Charged hadron multiplicity and transverse energy densities in PbPb collisions*
 358 *from CMS*, Journal of Physics G: Nuclear and Particle Physics **38** (2011) 124041 (cit. on p. 11).
- 359 [51] B. Muller, J. Schukraft and B. Wyslouch, *First Results from Pb+Pb collisions at the LHC*, Ann. Rev.
 360 Nucl. Part. Sci. **62** (2012) 361, arXiv: [1202.3233](#) [[hep-ex](#)] (cit. on p. 12).

- 361 [52] T. Sjostrand, S. Mrenna and P. Z. Skands, *A Brief Introduction to PYTHIA 8.1*, Comput. Phys.
 362 Commun. **178** (2008) 852, arXiv: [0710.3820 \[hep-ph\]](#) (cit. on p. 11).
- 363 [53] G.-Y. Qin and X.-N. Wang, *Jet quenching in high-energy heavy-ion collisions*, Int. J. Mod. Phys. E **24**
 364 (2015) 1530014, [,309(2016)], arXiv: [1511.00790 \[hep-ph\] \[hep-ph\]](#) (cit. on pp. 11, 12, 15).
- 365 [54] A. D. Martin, W. J. Stirling, R. S. Thorne and G. Watt, *Parton distributions for the LHC*, The European
 366 Physical Journal C **63** (2009) 189, ISSN: 1434-6052, URL: <https://doi.org/10.1140/epjc/s10052-009-1072-5> (cit. on p. 13).
- 368 [55] M. Hirai, S. Kumano and T.-H. Nagai, *Determination of nuclear parton distribution functions and*
 369 *their uncertainties at next-to-leading order*, Phys. Rev. C **76** (6 2007) 065207 (cit. on p. 14).
- 370 [56] D. de Florian and R. Sassot, *Nuclear parton distributions at next to leading order*, Phys. Rev. D **69** (7
 371 2004) 074028 (cit. on p. 14).
- 372 [57] K. Eskola, H Paukkunen and C. Salgado, *EPS09 — A new generation of NLO and LO nuclear parton*
 373 *distribution functions*, Journal of High Energy Physics **2009** (2009) 065 (cit. on p. 14).
- 374 [58] S. J. Brodsky and H. J. Lu, *Shadowing and antishadowing of nuclear structure functions*, Phys. Rev.
 375 Lett. **64** (12 1990) 1342 (cit. on p. 14).
- 376 [59] European Muon Collaboration, *The ratio of the nucleon structure functions F2N for iron and deuterium*,
 377 Physics Letters B **123** (1983) 275, ISSN: 0370-2693 (cit. on p. 14).
- 378 [60] O. Hen, E. Piasetzky and L. B. Weinstein, *New data strengthen the connection between short range*
 379 *correlations and the EMC effect*, Phys. Rev. C **85** (4 2012) 047301 (cit. on p. 14).
- 380 [61] K. Saito and T. Uchiyama, *Effect of the Fermi Motion on Nuclear Structure Functions and the Emc*
 381 *Effect*, Z. Phys. **A322** (1985) 299 (cit. on p. 14).
- 382 [62] CMS Collaboration, *Jet momentum dependence of jet quenching in PbPb collisions at sNN=2.76 TeV*,
 383 Physics Letters B **712** (2012) 176, ISSN: 0370-2693 (cit. on p. 14).
- 384 [63] ATLAS collaboration, *Study of inclusive jet yields in Pb+Pb collisions at $\sqrt{s_{NN}} = 5.02$ TeV*, (2017)
 385 (cit. on p. 14).
- 386 [64] The CMS collaboration, *Measurement of transverse momentum relative to dijet systems in PbPb and*
 387 *pp collisions at $\sqrt{s_{NN}} = 2.76$ TeV*, Journal of High Energy Physics **2016** (2016) 6, ISSN: 1029-8479, URL:
 388 [https://doi.org/10.1007/JHEP01\(2016\)006](https://doi.org/10.1007/JHEP01(2016)006) (cit. on p. 14).
- 389 [65] S. Chatrchyan et al., *Jet momentum dependence of jet quenching in PbPb collisions at $\sqrt{s_{NN}} = 2.76$*
 390 *TeV*, Phys. Lett. **B712** (2012) 176, arXiv: [1202.5022 \[nucl-ex\]](#) (cit. on p. 14).

- 391 [66] R. Baier, Y. Dokshitzer, A. Mueller, S. Peigné and D. Schiff, *Radiative energy loss of high energy quarks*
 392 *and gluons in a finite-volume quark-gluon plasma*, Nuclear Physics B **483** (1997) 291, ISSN: 0550-3213
 393 (cit. on p. 15).
- 394 [67] M. Gyulassy, P. Levai and I. Vitev, *Jet quenching in thin quark gluon plasmas. 1. Formalism*, Nucl.
 395 Phys. **B571** (2000) 197, arXiv: [hep-ph/9907461 \[hep-ph\]](#) (cit. on p. 15).
- 396 [68] U. A. Wiedemann, *Gluon radiation off hard quarks in a nuclear environment: Opacity expansion*, Nucl.
 397 Phys. **B588** (2000) 303, arXiv: [hep-ph/0005129 \[hep-ph\]](#) (cit. on p. 15).
- 398 [69] P. B. Arnold, G. D. Moore and L. G. Yaffe, *Photon emission from ultrarelativistic plasmas*, JHEP **11**
 399 (2001) 057, arXiv: [hep-ph/0109064 \[hep-ph\]](#) (cit. on p. 15).
- 400 [70] X.-F. Guo and X.-N. Wang, *Multiple scattering, parton energy loss and modified fragmentation functions*
 401 *in deeply inelastic e A scattering*, Phys. Rev. Lett. **85** (2000) 3591, arXiv: [hep-ph/0005044 \[hep-ph\]](#)
 402 (cit. on p. 15).
- 403 [71] M. Cacciari, G. P. Salam and G. Soyez, *The Anti- $k(t)$ jet clustering algorithm*, JHEP **0804** (2008) 063,
 404 arXiv: [0802.1189 \[hep-ph\]](#) (cit. on pp. 15, 16).
- 405 [72] S. Catani, Y. L. Dokshitzer, M. H. Seymour and B. R. Webber, *Longitudinally invariant K_t clustering*
 406 *algorithms for hadron hadron collisions*, Nucl. Phys. **B406** (1993) 187 (cit. on p. 16).
- 407 [73] Y. L. Dokshitzer, G. D. Leder, S. Moretti and B. R. Webber, *Better jet clustering algorithms*, JHEP
 408 **08** (1997) 001, arXiv: [hep-ph/9707323 \[hep-ph\]](#) (cit. on p. 16).
- 409 [74] G. P. Salam, *Towards Jetography*, Eur. Phys. J. **C67** (2010) 637, arXiv: [0906.1833 \[hep-ph\]](#) (cit. on
 410 pp. 16, 17).
- 411 [75] G. P. Salam and G. Soyez, *A practical seedless infrared-safe cone jet algorithm*, Journal of High Energy
 412 Physics **2007** (2007) 086 (cit. on p. 17).
- 413 [76] ATLAS Collaboration, *Measurement of the jet radius and transverse momentum dependence of inclusive*
 414 *jet suppression in lead-lead collisions at $\sqrt{s_{NN}} = 2.76$ TeV with the ATLAS detector*, Phys. Lett. **B719**
 415 (2013) 220, arXiv: [1208.1967 \[hep-ex\]](#) (cit. on p. 18).